

**N-Dopants Optimize the Utilization of Spontaneously Formed Photocharges in Organic Solar Cells**

Journal:	<i>Energy & Environmental Science</i>
Manuscript ID	EE-ART-11-2022-003612.R1
Article Type:	Paper
Date Submitted by the Author:	23-Dec-2022
Complete List of Authors:	Tang, Yabing; Xi'an Jiaotong University Zheng, Hong; Xi'an Jiaotong University Zhou, Xiaobo; Xi'an Jiaotong University Tang, Zheng; Center for Advanced Low-dimension Materials, Donghua University, Ma, Wei; Xi'an Jiaotong University, State Key Laboratory for Mechanical Behavior of Materials Yan, Han; Xi'an Jiaotong University, State Key Laboratory for Mechanical Behavior of Materials

The photo-excited states of organic semiconductors can be categorized into exciton, excimer, and intramolecular/intermolecular polaron pair. Theoretically, the polaron pair transforms into free carriers more efficiently than the exciton due to the larger extent of delocalization, which potentially produces higher power conversion efficiency in organic solar cells. Though the polaron pairs have been widely observed in conjugated polymers and small molecules, the low yield and short lifetime limits their contribution to the photovoltaic performance. During the past years, the emergence of non-fullerene small molecular acceptors brings rapid conversion efficiency progress with varying photocharge generation route. Taking the state-of-the-art Y6 as an example, the photocharges spontaneously form in neat Y6 at high yield without the assistance of donor/acceptor heterojunction. The spontaneous photocharges then separate at the heterojunction without passing by the intermediate charge-transfer state. The alternative route avoids the extra energy loss and loosens the fine requirement on hierarchical morphology of the active layer, which potentially overcomes the intrinsic limits on organic solar cells comparing with other photovoltaic techniques. However, to efficiently utilize the spontaneous photocharges, severe bimolecular recombination has to be alleviated before their spatial separation in distinct transporting pathways and in the following extraction process. Herein, we propose addition of n-dopant as a solution to the above problem. Calculation predicts that n-dopant addition can reduce the exciton binding energy and forms type II heterogeneity in Y6, which facilitate the spontaneous photocharge formation and suppress the occurrence of bimolecular recombination. The roles of n-dopant on the spontaneous photocharge in Y6 are systematically examined in the dilute heterojunction device with ultralow donor content and neat Y6 devices. Step further, we conduct the n-dopants benefits to high-efficiency device with 400 nm thick active layer, an average 10% enhancement of conversion efficiency promises it a feasible strategy on the development of commercial organic solar cells with printing manufacture procedure. Besides performance improvement, our findings open up the potential to think beyond the recognized heterojunction concept in organic photovoltaics and design one-component devices as other photovoltaic techniques. Our findings also provide a new mechanism view for the working principle of electric dopant-included organic solar cells.

ARTICLE

N-Dopants Optimize the Utilization of Spontaneously Formed Photocharges in Organic Solar Cells

Yabing Tang,^a Hong Zheng,^b Xiaobo Zhou,^a Zheng Tang,^c Wei Ma,^a and Han Yan^{*a}

Received 00th January 20xx,
Accepted 00th January 20xx

DOI: 10.1039/x0xx00000x

The non-fullerene acceptor (NFA) not only brings rapid efficiency progress to organic solar cell (OSC), but also arouses scientific interest in re-evaluating the photocharge generation route via spontaneous or heterojunction-assisted charge separation. Herein, we propose addition of n-dopants as a strategy to optimize the utilization of spontaneously formed photocharges in NFA, and construct ultralow donor-content dilute bulk heterojunction (BHJ) devices to validate the dopant's roles. N-dopant enhances the transport length of spontaneously formed photocharges over twofold and alleviates the bimolecular recombination with balanced carrier mobility during charge extraction. It improves the photocurrent of ultralow donor-content dilute BHJ devices over 2.4 times. Moreover, these benefits are successfully conducted to the BHJ devices, enhancement of conversion efficiencies are observed in both of the 100 nm and 400 nm thick OSCs. Our results provide a feasible way to optimize the intrinsic photocharges in NFA, and renew the possibility of efficient single-component OSC as the inorganic photovoltaic techniques.

Introduction

OSC promises renewable energy harvesting application in wearable electronics and power-generating windows at low cost. Organic semiconductors in these devices are molecular solids, which give rise to strong electron-phonon coupling due to the weak joint interactions and low dielectric permittivity. Therefore, the excited states after irradiation in organic semiconductors are Coulomb bounded electron-hole pairs named as Frenkel excitons (EXs). As a result, OSC is a type of excitonic photovoltaic devices which produces photocharges at the electron-donor/-acceptor (D/A) heterojunction driven by local electric potential offset. For efficient utilization of the Frenkel exciton, its diffusion length has to be taken into consideration, which restricts the component domain size in several tens of nanometers to form the BHJ structure. The requirements for D/A heterojunction with fine BHJ morphology bring extra energy loss and fabricating complexity to OSC comparing with other photovoltaic techniques.¹⁻⁴ Apparently, developing organic photovoltaic materials with the ability of spontaneous production of photocharges is a promising strategy to overcome the intrinsic limit in OSC and make it competitive in commercial application.

During the past decade, ultrafast exciton delocalization and splitting in neat materials have been observed in conjugated polymers and organic molecules.^{5,6} Fundamentally, the uncertainty associated with the photon absorption process leads to initial exciton delocalization with size of $\lambda/4\pi$.⁷ In addition, the excess energy of photon is able to produce hot charge-transfer (CT) exciton which undergoes activationless separation within 100 fs.⁸ The push-pull monomers of copolymers and small molecules stabilize the intramolecular exciton delocalization to form polaron pair.⁹ Further inserting the π -conjugated spacers between them is able to enhance the yield of exciton splitting by reducing the intramolecular polaron pair recombination.¹⁰ The semi-crystalline structure with well-defined interfaces between amorphous and crystalline domains facilitate intermolecular exciton splitting and polaron pair formation.¹¹ Although it has been confirmed that these short-lived hot excitons in neat materials help overcome the large EX binding energy and set the time limit for charge separation at D/A heterojunction,¹² the low yield (<30%) compared with the total excited states restricts their contribution to the overall photocharges in OSC.¹³

The rapid development of NFAs not only refreshes the power conversion efficiency (PCE) record of OSC, but also brings new photo-physical properties in the photovoltaic process. The state-of-the-art 2,2'-((2Z,2'Z)-((12,13-bis(2-ethylhexyl)-3,9-diundecyl)-12,13-dihydro-[1,2,5]thiadiazolo[3,4-e]thieno[2'',3'':4',5']thieno[2',3':4,5]pyrrolo[3,2-g]thieno[2',3':4,5]thieno[3,2-b]indole-2,10-diyl)bis(methanylylidene))bis(5,6-difluoro-3-oxo2,3-dihydro-1H-indene-2,1-diylidene))dimalononitrile (Y6, Fig. S1, ESI[†]) has remarkable small EX binding energy of -0.11-0.15 eV due to strong charge polarization effects,¹⁴ which leads to 60-90% of intrinsic photocharges in neat films following by spatial separation at D/A heterojunction

^a State Key Laboratory for Mechanical Behavior of Materials, School of Materials Science and Engineering, Xi'an Jiaotong University, Xi'an 710049, China. E-mail: mseyanhan@xjtu.edu.cn

^b Center of Nanomaterials for Renewable Energy, State Key Laboratory of Electrical Insulation and Power Equipment, School of Electrical Engineering, Xi'an Jiaotong University, Xi'an 710049, China

^c Center for Advanced Low-dimension Materials, State Key Laboratory for Modification of Chemical Fibers and Polymer Materials, College of Materials Science and Engineering, Donghua University, Shanghai 201620, China
Electronic Supplementary Information (ESI) available: Details of experiments and calculations; supplementary figures, supplementary tables, and supplementary references. See DOI: 10.1039/x0xx00000x

without passing by the traditional CT state.¹⁵ For clarity, the altered route for photocharges in Y6-based OSCs is visualized in Fig. 1a and 1b. The EX directly transforms to charge-separation (CS) state in Y6 and then spatially splits into free carrier (FC) in D and A phases (Route 2 in Fig. 1b) as compared to the traditional EX diffusion and splitting via an intermediate CT state (Route 1 in Fig. 1a). Although the revolution of photocharge generation route indicates that the D/A heterojunction might be no longer necessary for efficient OSC just like its inorganic counterparts, severe bimolecular recombination due to the lack of respective extraction pathways is a major obstacle for achieving considerable PCE value in single-component OSC device.^{15,16}

Results and discussion

Since the bimolecular recombination coefficient in OSC is related to the probability of opposite photocharges encounters, constructing the spatial isolation of holes and electrons by type II heterogeneity and balanced carrier mobility during extraction are key points to alleviate the photocharge loss. Much efforts have been devoted to prove that the addition of molecular dopants is a powerful tool to optimize the electronic structure and electrical properties of organic semiconductors.¹⁷⁻²³ Considering the lower electron mobility as compared to the hole mobility in Y6,^{18,24} herein we adopt n-dopants to alleviate the bimolecular recombination in neat film. We run density functional theory (DFT) calculations to predict the energy level shift of Y6 dimers after (4-(1,3-dimethyl-2,3-dihydro-1H-benzimidazol-2-yl)phenyl)dimethylamine (N-DMBI, Fig. S1, ESI[†]) addition, where the computational details are given in electronic supplementary information. According to recent findings, we assume that N-DMBI reacts with Y6 via initial hydride transfer,²⁵⁻²⁷ which may further transform to $[Y6]^{\bullet-} + [Y6-H]^{\bullet+}$ to complete the doping process.²⁷ In simplicity, we calculate the possible reaction on Y6 dimer by merely considering the first reaction step with products of Y6-Y6, $[Y6-Y6H]^{-}$ and $N-DMBI^{+}$ (Fig. 2a). The optimized three-dimensional structure demonstrates that the $N-DMBI^{+}$ locates above the π - π stacked Y6 dimer (Fig. 2b). Under the optimal conformation, the ionization potential (IP) and electron affinity (EA) of the Y6 dimer separately shifts from 6.81 eV to 4.80 eV, and from 2.71 eV to 2.27 eV after N-DMBI addition. As a result, the energy level offsets between pristine and N-DMBI added regimes enable the formation of type II heterogeneity in Y6 film, which potentially alleviates the photocharge recombination (Fig. 2c). The obstacle for photocharge generation is evaluated by calculating the exciton binding energy (E_b), which is derived from the energy difference between the optical gap (E_g^o) and transport gap (E_g^t).²⁸ The E_g^o is the excitation energy of the first singlet excited state and the E_g^t is the energy difference between IP and EA. The E_b of Y6 dimer reduces from 1.79 eV to 1.01 eV after N-DMBI addition (Table S1, ESI[†]). Apparently, the lower E_b with type II heterogeneity formation are good for the utilization of spontaneous photocharges in neat Y6, and it is urgent to figure it out in real device.

To examine the n-dopant's benefits on the CS route in Y6, we adopt ultralow donor-content dilute BHJ structure with 1% concentration of poly[(2,6-(4,8-bis(5-(2-ethylhexyl)-3-fluoro)thiophen-2-yl)-benzo[1,2-b:4,5-b']dithiophene))-alt-

(5,5-(1',3'-di-2-thienyl-5',7'-bis(2-ethylhexyl)benzo[1',2'-c:4',5'-c']dithiophene-4,8-dione)) (PM6, Fig. S1, ESI[†]) as a study model. Comparing with the BHJ structure, we choose this model for three reasons: first, PM6 disperses uniformly in Y6 matrix at ultralow content,²⁹ which inhibits the n-dopant incorrectly locating in PM6 aggregates; second, the dilute PM6 concentration in blend film reduces the net contribution of electron-transfer to short-circuit current (J_{sc}), which simplifies the photocharge generation process for mechanism study; Finally, the products and dynamics of the excited states in ultralow donor content dilute BHJ film are similar with the neat Y6 film, which makes it an ideal test bed for the Route 2 contribution to device performance.¹⁵ We compare the morphologies of the pristine and N-DMBI added PM6:Y6 (0.01:1) films from grazing incident wide-angle X-ray scattering (GIWAXS) measurements (Fig. 3a, S2 and Table S2, ESI[†]) before looking into the n-dopant's influences on photovoltaic performance. The Y6 adopts predominantly face-on orientation to the substrate in both of the pristine and N-DMBI added films. Fitting the diffraction peaks at 1.76 \AA^{-1} to 1.77 \AA^{-1} in the out of plane direction separately provides the π - π stacking information before and after N-DMBI addition. The corresponding π - π distances of 3.56 \AA and 3.55 \AA with similar coherence length of 2.85 nm and 2.83 nm demonstrate little influence of N-DMBI on the dilute film morphology. The coexistence of Route 1 & 2 in the dilute BHJ film is confirmed by temperature-dependent photoluminescence (PL) spectrum measurement,^{14,30,31} since CS in neat Y6 domain and PM6/Y6 heterojunction show distinct intensity-varying trends when cooling from room temperature (Fig. S3, ESI[†]). The enhanced integrated PL intensity with increased temperature demonstrates spontaneous CS formation in neat Y6 film (Fig. 3b). Whereas the integrated PL intensity starts decreasing at 220 K with high residual intensity at room temperature, indicating that besides a part of EXs quench at PM6/Y6 heterojunction, the rest EXs undergo spontaneous CS in Y6 domains of the ultralow PM6-content dilute BHJ film (Fig. 3b).^{15,32} As a result, we are able to evaluate the n-dopant's effects on photocharge generation process of Y6 in the ultralow donor-content dilute BHJ samples (Fig. 3c).

We then fabricate photovoltaic devices to test the n-dopant's effects on photocharge generation. It is impressive that N-DMBI averagely enhances the J_{sc} by 2.4 times in 1% PM6-content dilute BHJ devices, from 2.02 mA cm^{-2} to 4.82 mA cm^{-2} , with slight open-circuit voltage (V_{oc}) increment from 0.844 V to 0.856 V (Fig. 3d and Table S3, ESI[†]). The significant J_{sc} variation is well supported by the integrated current densities from external quantum efficiency (EQE) measurements, where it increases from 2.09 mA cm^{-2} to 4.99 mA cm^{-2} (Fig. S4, ESI[†]). We also fabricate the single component (Y6) devices to verify this phenomenon, where we observe that all three photovoltaic parameters are improved when 0.5 wt% N-DMBI is added (Table S4, ESI[†]). The PCE averagely increases from 0.07 % to 0.11 %, along with the improved V_{oc} (from 0.841 V to 0.868 V), J_{sc} (from 0.25 mA cm^{-2} to 0.30 mA cm^{-2}), and FF (from 32.3 % to 34.4 %). Further increasing the n-dopant content leads to much higher J_{sc} but sacrificed V_{oc} and FF. The champion PCE of 0.13 % is obtained with the addition of 2 wt% N-DMBI, accompanying with 2.5 times higher J_{sc} of 0.62 mA cm^{-2} (Fig. 3e and Table S4, ESI[†]). Leaving the J_{sc} enhancement for later

discussion, we estimate the energy loss to explain the slight V_{oc} raise of the ultralow donor-content dilute BHJ device after doping. Noticing that the photovoltaic performance contribution in Route 2 doesn't pass by CT state, we calculate E_g^{PV} (photovoltaic band-gap energy), V_{oc}^{SQ} (the maximum voltage deduced by the Shockley-Queisser theory), and V_{oc}^{rad} (the V_{oc} when only radiative recombination occurs) to evaluate the energy loss (Fig. S5, ESI[†]).^{33,34} We give a detailed description on the calculation of E_g^{PV} , V_{oc}^{SQ} and V_{oc}^{rad} in electronic supplementary information, and the non-radiative voltage loss (ΔV_{nrad}) is obtained from the electroluminescence EQE (EQE_{EL}) (Fig. 3f). Based on the analysis of each value in Table S5 (ESI[†]), we conclude that the reduced ΔV_{nrad} is responsible for the V_{oc} raise. We emphasize that even the photocharges spontaneously form without the aid of CT state at D/A heterojunction, reducing the ΔV_{nrad} is still crucial for device optimization.

We further extend our observations to other acceptor materials, such as L8-BO, BTP-eC9, ITIC, and IEICO (see their full names and chemical structures in Fig. S1, ESI[†]). The addition of N-DMBI is good for all material combinations in dilute BHJ devices with PM6:NFA ratio of 0.01:1 (Fig. 3g). The L8-BO and BTP-eC9 based dilute devices exhibit relatively higher original J_{sc} and PCE than the ITIC and IEICO based devices probably due to their higher FC yield.¹⁴ Addition of 0.05 wt% N-DMBI content largely increase the J_{sc} from 1.49 mA cm⁻² to 2.22 mA cm⁻², and from 2.10 mA cm⁻² to 3.61 mA cm⁻² in L8-BO and BTP-eC9 based dilute devices. Together with slightly higher V_{oc} , the PCE values increase by 1.3 (from 0.70 % to 0.91 % for L8-BO) and 1.8 times (from 0.64 % to 1.15 % for BTP-eC9) correspondingly (Fig. S6a, S6b, Table S6 and S7, ESI[†]). As for ITIC based 1% PM6-content dilute blend devices, 1.8 times higher average PCE (from 0.09 % to 0.16 %) mainly ascribing from J_{sc} increment (from 0.38 mA cm⁻² to 0.60 mA cm⁻²) is observed with the addition of 0.05 wt% N-DMBI (Figure S6c and Table S8, ESI[†]). The most impressive PCE enhancement comes from IEICO based dilute BHJ devices with the lowest initial performance. The large addition of 0.5 wt% N-DMBI synergistically helps J_{sc} increase from 0.14 mA cm⁻² to 1.17 mA cm⁻², and V_{oc} increase from 0.526 V to 0.732 V, producing an overall PCE enhancement by 11.5 times from merely 0.02% to 0.23% (Figure S6d and Table S9, ESI[†]).

The alteration of n-dopants retains the performance enhancement in PM6 diluted devices, DMBI-BCZC (see full name and chemical structure in Fig. S1, ESI[†]), which is a simple electron donor with sufficient strength to reduce Y6, and TBAI (see full name and chemical structure in Fig. S1, ESI[†]), which may react through nucleophilic attack by iodide with follow-on reactions. Using a bulky dopant DMBI-BCZC, the PCE improves to 1.34% mainly due to the 2.1 times J_{sc} enhancement of 4.28 mA cm⁻² (Fig. 3h, S7 and Table S10, ESI[†]). An organic salt TBAI also makes a good J_{sc} (4.41 mA cm⁻²) enhancement by 2.2 times (Fig. 3h, S7 and Table S10, ESI[†]). Based on the above studies, we are confident that the n-dopants generally boost the photovoltaic performance through optimizing the non-fullerene acceptors.

Before discussing the fundamentals on J_{sc} enhancement, we have to confirm that it occurs in the photogeneration process. To exclude the effects of dopant on higher background charge density, we compare the dark J - V curves

with and without N-DMBI added devices (Fig. S8, ESI[†]). The lower dark current demonstrates that it is the photocurrent rather than the dark current responsible for the J_{sc} enhancement. To further understand the n-dopant's effect on raised photogenerated J_{sc} , it is prior to clarify which photocharge generation routes contribute to its enhancement after n-dopant addition. Considering the high EX splitting efficiency at PM6/Y6 heterojunction, scientists have attributed the success of this material pair to long exciton diffusion length (L_{EX}).^{35,36} Therefore, we first extract the L_{EX} by film thickness varying PL measurements.³⁷⁻³⁹ As schemed in Fig. 4a, the PL method detects the signals from emitted EXs that fail to arrive at the Y6/copper(I) thiocyanate (CuSCN) heterojunction, and it is fitted by the following equation according to previous report:

$$\frac{PL_{Y6/CuSCN}}{PL_{Y6}} = 1 - \frac{L_{EX}}{x_0} \tanh\left(\frac{x_0}{L_{EX}}\right)$$

where $PL_{Y6/CuSCN}$ is the integrated PL intensity of Y6/CuSCN bilayer film, PL_{Y6} is the integrated PL intensity of neat Y6 film, and x_0 is the film thickness of Y6 layer (see details in electronic supplementary information). We find that the L_{EX} of Y6 keeps a constant of 11 nm after 0.1 wt% N-DMBI addition (Fig. 4b and S9, ESI[†]). The unchanged L_{EX} implies that the photocharge generation via Route 1 is not responsible for the enhanced J_{sc} in the n-dopant addition case. To examine the photocharge generation via Route 2, we extract the sum of EX and CS states transport length (L_{EX+CS}) by film thickness varying EQE measurements.⁴⁰⁻⁴² As schemed in Fig. 4a, the EQE method detects the signals from EX and CS states that successfully arrive at the Y6/CuSCN heterojunction, and it is extracted by one-dimensional diffusion equation in device structure of ITO/CuSCN/Y6/(2 - (1,10 - phenanthrolin - 3 - yl)naphth - 6 - yl)diphenylphosphine oxide (Phen-NaDPO)/Al (see details in electronic supplementary information):

$$\left(\frac{\partial^2}{\partial x^2} - \frac{1}{L_{EX+CS}^2}\right)n(x) = -\frac{G(x)}{D}$$

where $n(x)$ is the exciton density n at position x in Y6 film, D is the diffusion coefficient, $G(x)$ is the exciton generation profile at position x calculation by transfer-matrix model (parameters for calculation are listed in Fig. S10 in electronic supplementary information according to previous report). With the boundary conditions of complete exciton quenching at Y6/CuSCN interface ($n=0$) and complete exciton reflection at Y6/Phen-DPO interface ($\partial n/\partial x=0$), we can obtain the general solution of $D \cdot n(x)$ with the unknown parameter L_{EX+CS} , which is related to the photovoltaic EQE spectra according to:

$$EQE = \frac{q\eta_c D \partial n(x)}{J_{inc} \partial x} \Big|_{Y6/CuSCN \text{ interface}}$$

where J_{inc} is the incident light current density, η_c is exciton splitting and extraction efficiencies at the electrode. The shapes of EQE spectra at various film thicknesses are only influenced by the value of L_{EX+CS} , therefore the L_{EX+CS} can be extracted by fitting the experimentally obtained normalized EQE spectra. Based on the EQE plots in Fig. S11 (ESI[†]), we obtain the L_{EX+CS} at different exciting wavelengths from 600 nm to 800 nm (Fig. 4c and S12, ESI[†]). At all exciting wavelengths, the L_{EX+CS} increases from 35 nm to 80 nm after

N-DMBI addition, which indicates that the enhanced utilization of CS states is the reason for better J_{sc} .

According to recent progresses from Hodgkiss and Liu et al., the severe bimolecular recombination dominates the performance loss in neat Y6 and ultralow donor-content dilute PM6/Y6 films.^{15,43} We next look into the role of n-dopant on spontaneous photocharge bimolecular recombination in the framework of 1% PM6-content dilute BHJ devices. We assume that the asymmetric composition of the dilute BHJ film leads to unbalanced carrier extraction ability, and severe bimolecular recombination occurs due to formation of space-charge region. The assumption is supported by exponentially fitting the $J_{sc} \propto P^\beta$ (P represents the light-intensity) relationship on double-logarithm scale. The coefficient β is 0.78 for the undoped dilute film, which is close to the value of 0.75 when the charge extraction is limited by the space-charge region.⁴⁴ After n-dopant addition, β increases to 0.84, suggesting that the space-charge region is partially compensated (Fig. 4d). Accompanying with this, we find that the hole mobility decreases averagely from $2.67 \pm 1.38 \times 10^{-4} \text{ cm}^2 \text{V}^{-1} \text{ s}^{-1}$ to $1.50 \pm 0.59 \times 10^{-4} \text{ cm}^2 \text{V}^{-1} \text{ s}^{-1}$, while the electron mobility increases averagely from $0.87 \pm 0.16 \times 10^{-4} \text{ cm}^2 \text{V}^{-1} \text{ s}^{-1}$ to $1.42 \pm 0.46 \times 10^{-4} \text{ cm}^2 \text{V}^{-1} \text{ s}^{-1}$ (Fig. 4e and 4f, Table S11, ESI[†]). We ascribe the balanced mobility as the reason for n-dopant led minimized space-charge region and suppressed bimolecular recombination. According to the hopping model, energy disorder (σ) plays a vital role on charge transport in organic semiconductors. It can be estimated from the slope of 0-0 peak ($\sim 970 \text{ nm}$) vs $1/T$.^{45,46} In accordance with the activated diffusion model,⁴⁵ two temperature regimes are observed. We find that the σ of Y6 reduces in both regimes (Fig. S13, ESI[†]). The lower σ can be explained by the n-doping induced electron transfer from N-DMBI to the lowest unoccupied molecular orbital (LUMO) of Y6. Since the LUMO of Y6 provides transport energy level for electrons, we ascribe the lower σ of Y6 as the reason for better electron mobility.

To further correlate the enhanced CS state transport distance with the reduced photocharge recombination, we calculate the drift ($L_{Dr,CS}$) and diffusion ($L_{Dif,CS}$) lengths of CS state in the ultralow donor-content dilute BHJ device. The $L_{Dr,CS}$ can be deduced from the figure of merits (FoM) ϑ according to:^{47,48}

$$L_{Dr,CS} = \sqrt{\frac{x_0^2}{\theta}} = \sqrt{\frac{q\mu_n\mu_p V_{int}}{\gamma x_0 J_{sat}}}$$

where ϑ represents for the ratio of recombination to extraction rates, q is the elemental charge, V_{int} is the internal voltage, μ_n and μ_p are the electron and hole mobilities, γ is the bimolecular recombination coefficient, and J_{sat} is the saturated photocurrent at sufficient negative bias (Fig. S14, ESI[†]). Based on the measurements of above parameters, the FoM ϑ decreases from 3.3×10^{-2} to 1.7×10^{-2} after N-DMBI addition, which produces longer $L_{Dr,CS}$ from 358 nm to 596 nm (Fig. 4g). We further calculate the $L_{Dif,CS}$ according to the FoM α following by:^{47,49}

$$L_{Dif,CS} = \sqrt{\frac{x_0^2}{2\alpha}} = \left(\frac{\mu_n\mu_p (k_B T)^2 x_0}{q\gamma J_{sat}} \right)^{\frac{1}{4}}$$

where α reflects the balance between photocharge recombination and extraction in transport-limited solar cells, k_B is the Boltzmann constant, and T is the temperature. The

FoM α decreases from 3.0 to 2.2 after N-DMBI addition, and the $L_{Dif,CS}$ correspondingly increases from 15.6 nm to 25.3 nm (Fig. 4h). Since the L_{EX+CS} lays between the $L_{Dr,CS}$ and $L_{Dif,CS}$, and its over twofold increment is larger than any improvement of $L_{Dr,CS}$ and $L_{Dif,CS}$, we believe that both factors contribute to the optimized photocharge extraction after n-dopant addition. We argue that the significantly enlarged $L_{Dr,CS}$ and $L_{Dif,CS}$ cannot be solely explained by the charge mobility variation, and the formation of type II heterogeneity should play a vital role. The n-dopant bound Y6 possesses up-shifted IP and EA, forming a temporary reservoir for holes. The shallow hole reservoir isolates holes from electrons in neat Y6 domains (Fig. 4e), thereby slows down the bimolecular recombination rate.^{15,43}

Having identified the roles of n-dopant on spontaneous photocharge generation and recombination in the model of ultralow donor-content dilute BHJ device, we then explore its potential in high-efficiency BHJ devices. To guarantee the correct N-DMBI doping sites in Y6, the BHJ devices are fabricated via sequential fabrication procedure as schemed in Fig. 5a. The combination between N-DMBI and Y6 occurs in chloroform solution as our previous finding.¹⁸ At normal BHJ film thickness of 100 nm, addition of N-DMBI leads to the average PCE value increasing from 16.09 % to 16.70 %, deriving from the simultaneous improvements on J_{sc} from 25.62 mA cm^{-2} to 26.43 mA cm^{-2} , and V_{oc} from 0.823 V to 0.829 V (Fig. 5b, Table 1 and S12, ESI[†]). The J_{sc} improvement is consistent with the integrated current density from EQE curves in Fig. 5c, where it increases from 24.37 mA cm^{-2} to 25.20 mA cm^{-2} . We also fabricate the BHJ devices via coating from the dopant contained blend solution. The similar performance improvement shows the good applicability of dopant addition method in conventional single-step deposition process (Fig. S15 and Table S13, ESI[†]). To extend the significance of n-dopant, we further investigate its effectiveness in thick-film devices. The thick film usually undergoes longer morphology evolution time, which results in larger phase separation with higher crystallinity.⁵⁰ This phenomenon is manifested as higher film roughness from 0.89 nm to 1.00 nm in the insets of Fig. 5b and 5d, and larger average surface height in Fig. S16 (ESI[†]). In addition, N-DMBI addition impacts neither the values of surface roughness nor the average height of the blend film, demonstrating the performance improvement is not from the morphology optimization. Beyond the 100 nm thin film, the addition of n-dopant works even better in thick films which are vital for printing fabrication. In the 300 nm active layer devices, the PCE value increases from 13.31 % to 14.19 %, along with simultaneously improved J_{sc} (from 27.28 mA cm^{-2} to 27.90 mA cm^{-2}) and V_{oc} (from 0.796 V to 0.804 V) (Fig. S17 and Table S14, ESI[†]). Further increasing the active layer thickness to 400 nm, N-DMBI enhances the PCE value with larger extent from 11.88% to 13.03% with thickness insensitive J_{sc} of 27.91 mA cm^{-2} (Fig. 5d, Table 1 and S15, ESI[†]). The integrated current density from the EQE plot agrees well with the J_{sc} within 5% deviation, where it increases from 25.26 mA cm^{-2} to 26.51 mA cm^{-2} (Fig. 5e). The promising results in thick devices demonstrates the inclusion of n-dopants as an applicable strategy in future commercial OSC manufacture.

Besides the PCE value, it is also important to evaluate the device stability. The strong quadrupole moment and long

alkyl side-chains promote the close packing of Y6 molecules.⁵¹ This confines the conformational change due to photoisomerization of vinyl groups,⁵² therefore Y6 demonstrates good photo-stability than other non-fullerene acceptors, such as ITIC. We measured the dark storage- and photo-stability of the photovoltaic cells. Since the pristine devices demonstrate poor stability in conventional structure in comparison with that in inverted structure (Fig. S18, ESI[†]), we adopt the latter form to evaluate the photovoltaic stability in n-dopant added cells. After 300 h dark storage in air, the PCE and J_{sc} of n-dopant added devices retain over 95% of their initial values (Fig. S18a and S18b, ESI[†]). Meantime, the performances are still higher than the pristine cells. Soaking in one Sun light, the devices still show good stability, where 90% of the initial PCE and J_{sc} is conserved after 300 h aging (Fig. S18c and S18d, ESI[†]). In accordance with our theoretical analysis, n-dopant addition does not accelerate the performance decay in doped devices (Fig. S19, ESI[†]).

Conclusions

In summary, we propose addition of n-dopant as a powerful tool to optimize the utilization of spontaneously formed photocharges in NFA. The DFT calculations predict the n-dopant's roles as reduced E_b and alleviated bimolecular recombination via formation of type II heterogeneity in neat Y6 film. In order to validate the assumptions on n-dopant, we adopt ultralow donor-content dilute BHJ film with low concentration of PM6 as a test bed. The transport length analysis on the thickness varying PL and EQE spectra confirms that the n-dopant actually favors the spontaneous photocharge in Y6 rather than the bound EX. Combining with the prolonged $L_{Dr,CS}$ and $L_{Dif,CS}$ led better charge extraction ability, the n-dopant addition produces an impressive J_{sc} increment over twofold in dilute BHJ devices. This phenomenon is also extended to other acceptor materials and n-dopants. With all of these benefits, n-dopant successfully improves the photovoltaic performance in lab used 100 nm thick and manufacture applicable 400 nm thick BHJ devices without destroying the stability. This work clarifies the controversial role of molecular dopant in high-performed NFA OSC and invokes attention on rethinking the long-time accepted photo-physics in organic photovoltaic process. The knowledge opens new space for PCE enhancement, and inspires record-breaking cells when bringing it into the existed champion devices.^{3,4} The findings open up the potential to think beyond the recognized BHJ concept and guide to design efficient single-component OSC without the excitonic limitations.

Author Contributions

H.Y. conceived and designed the research. Y.T. performed the experiments, including the device fabrication, exciton & electric measurements, AFM and PL characterizations. H.Z. run the DFT calculation. X.Z and Z.T. performed the sEQE and EQE_{EL} tests. Y. T.

drafted the manuscript, and H.Y. revised the manuscript. H. Y. and W. M. mentored the other authors throughout the investigation.

Conflicts of interest

There are no conflicts to declare.

Acknowledgements

Thanks for the support from the National Natural Science Foundation of China (21975198), the Key Scientific and Technological Innovation Team Project of Shaanxi Province (2020TD-002), and 111 project 2.0 (BP2018008). X-ray data was acquired at beamlines 7.3.3 at the Advanced Light Source, which is supported by the Director, Office of Science, Office of Basic Energy Sciences, of the U.S. Department of Energy under Contract No. DE-AC02-05CH11231. The authors thank Chenhui Zhu at beamline 7.3.3 for assistance with data acquisition.

Notes and references

- V. Coropceanu, X.-K. Chen, T. Wang, Z. Zheng and J.-L. Brédas, *Nat. Rev. Mater.* 2019, **4**, 689-707.
- X.-K. Chen, D. Qian, Y. Wang, T. Kirchartz, W. Tress, H. Yao, J. Yuan, M. Hülsbeck, M. Zhang, Y. Zou, Y. Sun, Y. Li, J. Hou, O. Inganäs, V. Coropceanu, J.-L. Brédas and F. Gao, *Nat. Energy* 2021, **6**, 799-806.
- L. Zhu, M. Zhang, J. Xu, C. Li, J. Yan, G. Zhou, W. Zhong, T. Hao, J. Song, X. Xue, Z. Zhou, R. Zeng, H. Zhu, C. Chen, R. C. I. MacKenzie, Y. Zou, J. Nelson, Y. Zhang, Y. Sun and F. Liu, *Nat. Mater.* 2022, **21**, 656-663.
- W. Gao, F. Qi, Z. Peng, F. R. Lin, K. Jiang, C. Zhong, W. Kaminsky, Z. Guan, C.-S. Lee, T. J. Marks, H. Ade and A. K.-Y. Jen, *Adv. Mater.* 2022, **34**, 202202089.
- R. Tautz, E. D. Como, C. Wiebeler, G. Soavi, I. Dumsch, N. Fröhlich, G. Grancini, S. Allard, U. Scherf, G. Cerullo, S. Schumacher and J. Feldmann, *J. Am. Chem. Soc.* 2013, **135**, 4282-4290.
- O. V. Kozlov, Y. N. Luponosov, A. N. Solodukhin, B. Flament, Y. Olivier, R. Lazzaroni, J. Cornil, S. A. Ponomarenko and M. S. Pshenichnikov, *Adv. Optical Mater.* 2017, **5**, 1700024.
- L. G. Kaake, J. J. Jasieniak, R. C. Bakus, G. C. Welch, D. Moses, G. C. Bazan and A. J. Heeger, *J. Am. Chem. Soc.* 2012, **134**, 19828-19838.
- N. Banerji, *J. Mater. Chem. C* 2013, **1**, 3052.
- B. S. Rolczynski, J. M. Szarko, H. J. Son, L. Yu and L. X. Chen, *J. Phys. Chem. Lett.* 2014, **5**, 1856-1863.
- R. Tautz, E. D. Como, T. Limmer, J. Feldmann, H.-J. Egelhaaf, E. v. Hauff, V. Lemaure, D. Beljonne, S. Yilmaz, I. Dumsch, S. Allard and U. Scherf, *Nat. Commun.* 2012, **3**, 970.
- O. G. Reid, J. A. N. Malik, G. Latini, S. Dayal, N. Kopidakis, C. Silva, N. Stingelin and G. Rumbles, *J. Polym. Sci., Part B: Polym. Phys.* 2012, **50**, 27-37.
- A. E. Jailaubekov, A. P. Willard, J. R. Tritsch, W.-L. Chan, N. Sai, R. Gearba, L. G. Kaake, K. J. Williams, K. Leung, P. J. Rossky and X.-Y. Zhu, *Nat. Mater.* 2013, **12**, 66-73.
- F. Paquin, G. Latini, M. Sakowicz, P.-L. Karsenti, L. Wang, D. Beljonne, N. Stingelin and C. Silva, *Phys. Rev. Lett.* 2011, **106**, 197401.

- 14 L. Zhu, J. Zhang, Y. Guo, C. Yang, Y. Yi and Z. Wei, *Angew. Chem. Int. Ed.* 2021, **60**, 15348-15353.
- 15 M. B. Price, P. A. Hume, A. Ilina, I. Wagner, R. R. Tamming, K. E. Thorn, W. Jiao, A. Goldingay, P. J. Conaghan, G. Lakhwani, N. J. L. K. Davis, Y. Wang, P. Xue, H. Lu, K. Chen, X. Zhan and J. M. Hodgkiss, *Nat. Commun.* 2022, **13**, 2827.
- 16 S. J. Lou, S. Loser, K. A. Luck, N. Zhou, M. J. Leonardi, A. Timalsina, E. F. Manley, D. Hayes, J. Strzalka, M. C. Hersam, R. P. H. Chang, T. J. Marks and L. X. Chen, *J. Mater. Chem. C* 2020, **8**, 15234.
- 17 Y. Tang, B. Lin, H. Zhao, T. Li, W. Ma and H. Yan, *ACS Appl. Mater. Interfaces* 2020, **12**, 13021-13028.
- 18 Y. Tang, H. Zheng, X. Zhou, Z. Tang, W. Ma and H. Yan, *Small Methods* 2022, **6**, 2101570.
- 19 W. Xue, Y. Tang, X. Zhou, Z. Tang, H. Zhao, T. Li, L. Zhang, S. Liu, C. Zhao, W. Ma and H. Yan, *Adv. Funct. Mater.* 2021, **31**, 2101892.
- 20 H. Yan, Y. Tang, X. Sui, Y. Liu, B. Gao, X. Liu, S. F. Liu, J. Hou and W. Ma, *ACS Energy Lett.* 2019, **4**, 1356-1363.
- 21 H. Yan, J. Chen, K. Zhou, Y. Tang, X. Meng, X. Xu and W. Ma, *Adv. Energy Mater.* 2018, **8**, 1703672.
- 22 H. Yan and W. Ma, *Adv. Funct. Mater.* 2022, **32**, 2111351.
- 23 Z. Chen, Y. Tang, B. Lin, H. Zhao, T. Li, T. Min, H. Yan and W. Ma, *ACS Appl. Mater. Interfaces* 2020, **12**, 25115-25124.
- 24 G. Zhang, X.-K. Chen, J. Xiao, P. C. Y. Chow, M. Ren, G. Kuppang, X. Jiao, C. C. S. Chan, X. Du, R. Xia, Z. Chen, J. Yuan, Y. Zhang, S. Zhang, Y. Liu, Y. Zou, H. Yan, K. S. Wong, V. Coropceanu, N. Li, C. J. Brabec, J.-L. Bredas, H.-L. Yip and Y. Cao, *Nat. Commun.* 2020, **11**, 3943.
- 25 Y. Zeng, W. Zheng, Y. Guo, G. Han and Y. Yi, *J. Mater. Chem. A* 2020, **8**, 8323.
- 26 B. D. Naab, S. Guo, S. Olthof, E. G. B. Evans, P. Wei, G. L. Millhauser, A. Kahn, S. Barlow, S. R. Marder, Z. Bao, *J. Am. Chem. Soc.* 2013, **135**, 15018-15025.
- 27 S. Jhulki, H.-I. Un, Y.-F. Ding, C. Risko, S. K. Mohapatra, J. Pei, S. Barlow, S. R. Marder, *Chem* 2021, **7**, 1050-1065.
- 28 L. Zhu, C. Yang, Y. Yi and Z. Wei, *J. Phys. Chem. Lett.* 2020, **11**, 10227-10232.
- 29 Y. Wang, M. B. Price, R. S. Bobba, H. Lu, J. Xue, Y. Wang, M. Li, A. Ilina, P. A. Hume, B. Jia, T. Li, Y. Zhang, N. J. L. K. Davis, Z. Tang, W. Ma, Q. Qiao, J. M. Hodgkiss, X. Zhan, *Adv. Mater.* 2022, <https://doi.org/10.1002/adma.202206717>.
- 30 Z.-A. Lan, G. Zhang, X. Chen, Y. Zhang, K. A. I. Zhang and X. Wang, *Angew. Chem. Int. Ed.* 2019, **58**, 10236-10240.
- 31 W. Xue, Z. Zhang, S. So, Y. Song, Z. Wei, W. Ma and H. Yan, *ACS Appl. Energy Mater.* 2022, **5**, 9929-9937.
- 32 R. Wang, C. Zhang, Q. Li, Z. Zhang, X. Wang and M. Xiao, *J. Am. Chem. Soc.* 2022, **142**, 12751-12759.
- 33 J. Benduhn, K. Tvingstedt, F. Piersimoni, S. Ullbrich, Y. Fan, M. Tropicano, K. A. McGarry, O. Zeika, M. K. Riede, C. J. Douglas, S. Barlow, S. R. Marder, N. Neher, D. Spoltore and K. Vandewal, *Nat. Energy* 2017, **2**, 17053.
- 34 J. Liu, S. Chen, D. Qian, B. Gautam, G. Yang, J. Zhao, J. Bergqvist, F. Zhang, W. Ma, H. Ade, O. Inganäs, K. Gundogdu, F. Gao and H. Yan, *Nat. Energy* 2016, **27**, 16089.
- 35 L. Perdigón-Toro, H. Zhang, A. Markina, J. Yuan, S. M. Hosseini, C. M. Wolff, G. Zuo, M. Stolterfoht, Y. Zou, F. Gao, D. Andrienko, S. Shoaee and D. Neher, *Adv. Mater.* 2020, **32**, 1906763.
- 36 P. Bi, S. Zhang, Z. Chen, Y. Xu, Y. Cui, T. Zhang, J. Ren, J. Qin, L. Hong, X. Hao and J. Hou, *Joule* 2021, **5**, 2408-2419.
- 37 Y. Tamai, H. Ohkita, H. Bente and S. Ito, *J. Phys. Chem. Lett.* 2015, **6**, 3417-3428.
- 38 D. E. Markov, E. Amsterdam, P. W. M. Blom, A. B. Sieval and J. C. Hummelen, *J. Phys. Chem. A* 2005, **109**, 5266-5274.
- 39 D. E. Markov, C. Tanase, P. W. M. Blom and J. Wildeman, *Phys. Rev. B* 2005, **72**, 045217.
- 40 Y. Firdaus, V. M. Le Corre, S. Karuthedath, W. Liu, A. Markina, W. Huang, S. Chattopadhyay, M. M. Nahid, M. I. Nugraha, Y. Lin, A. Seitkhan, A. Basu, W. Zhang, I. McCulloch, H. Ade, J. Labram, F. Laquai, D. Andrienko, L. J. A. Koster and T. D. Anthopoulos, *Nat. Commun.* 2020, **11**, 5220.
- 41 B. Siegmund, M. T. Sajjad, J. Widmer, D. Ray, C. Koerner, M. Riede, K. Leo, I. D. W. Samuel and K. Vandewal, *Adv. Mater.* 2016, **29**, 1604424.
- 42 S. Yoo, B. Domercq and B. Kippelen, *Appl. Phys. Lett.* 2004, **85**, 5427.
- 43 G. Zhou, M. Zhang, J. Xu, Y. Yang, T. Hao, L. Zhu, L. Zhou, H. Zhu, Y. Zou, G. Wei, Y. Zhang and F. Liu, *Energy Environ. Sci.* 2022, **15**, 3483-3493.
- 44 V. D. Mihailetschi, J. Wildeman and P. W. M. Blom, *Phys. Rev. Lett.* 2005, **94**, 126602.
- 45 S. Chandrabose, K. Chen, A. J. Barker, J. J. Sutton, S. K. K. Prasad, J. Zhu, J. Zhou, K. C. Gordon, Z. Xie, X. Zhan and J. M. Hodgkiss, *J. Am. Chem. Soc.* 2019, **141**, 6922-6929.
- 46 O. V. Mikhnenko, P. W. M. Blom and T.-Q. Nguyen, *Energy Environ. Sci.* 2015, **8**, 1867.
- 47 N. Tokmoldin, J. Vollbrecht, S. M. Hosseini, B. Sun, L. Perdigón-Toro, H. Y. Woo, Y. Zou, D. Neher and S. Shoaee, *Adv. Energy Mater.* 2021, **11**, 2100804.
- 48 D. Bartesaghi, I. d. C. Pérez, J. Kniepert, S. Roland, M. Turbiez, D. Neher and L. J. A. Koster, *Nat. Commun.* 2015, **6**, 7083.
- 49 D. Neher, J. Kniepert, A. Elimelech and L. J. A. Koster, *Sci. Rep.* 2016, **6**, 24861.
- 50 Y. Cai, Q. Li, G. Lu, H. S. Ryu, Y. Li, H. Jin, Z. Chen, Z. Tang, G. Lu, X. Hao, H. Y. Woo, C. Zhang and Y. Sun, *Nat. Commun.* 2022, **13**, 2369.
- 51 J. Luke, E. J. Yang, Y.-C. Chin, Y. Che, L. Winkler, D. Whatling, C. Labanti, S. Y. Park, and J.-S. Kim, *Adv. Energy Mater.* 2022, **12**, 2201267.
- 52 Z.-X. Liu, Z.-P. Yu, Z. Shen, C. He, T.-K. Lau, Z. Chen, H. Zhu, X. Lu, Z. Xie, H. Chen, C.-Z. Li, *Nat. Commun.* 2021, **12**, 3049.

ARTICLE

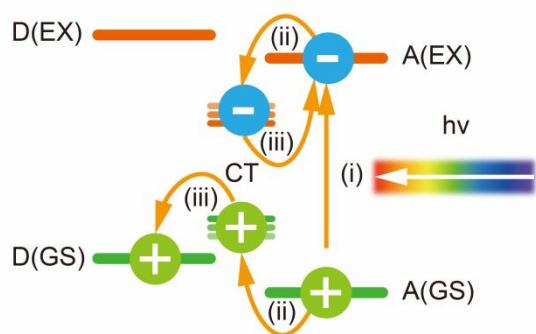
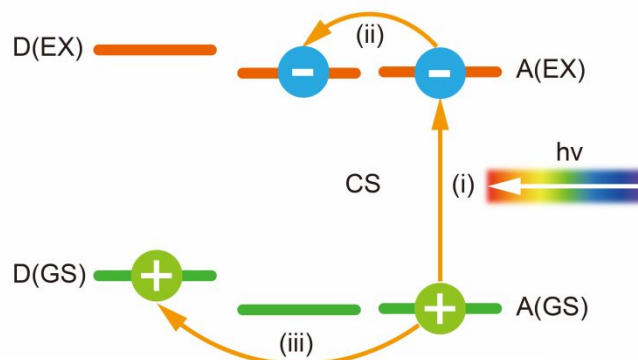
(a) Route 1: $EX \rightarrow CT \rightarrow FC$ (b) Route 2: $EX \rightarrow CS \rightarrow FC$ 

Fig. 1. The routes of photocharge generation in OSC: (a) The EX splits at D/A heterojunction via CT state. (i) The ground state (GS) Y6 molecular transforms to EX when it absorbs photons; (ii) the EX then forms CT exciton and (iii) splits into FC at D/A heterojunction. (b) The EX splits in Y6 and spatially transfers to distinct components at D/A heterojunction. The Y6 EX (i) spontaneously forms CS (ii), which then spatially splits into FC via direct charge transfer in D and A phases (iii).

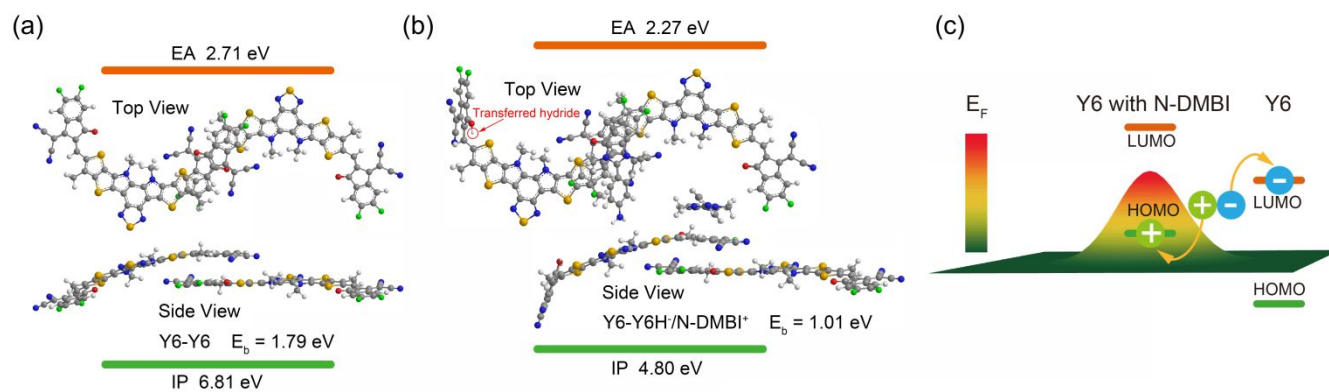


Fig. 2. (a-b) The optimal molecular conformations and energy levels of pristine and N-DMBI added Y6 dimers obtained from DFT calculations at the ω B97XD/6-31G(d)~LanL2DZ levels of theory: (a) pristine Y6 dimer, and (b) N-DMBI added Y6 dimer. (c) Scheme of the energy landscape of the N-DMBI included Y6 film, where the energy level offset between pristine and N-DMBI included molecules facilitates the spatial isolation of spontaneously formed holes and electrons in Y6.

ARTICLE

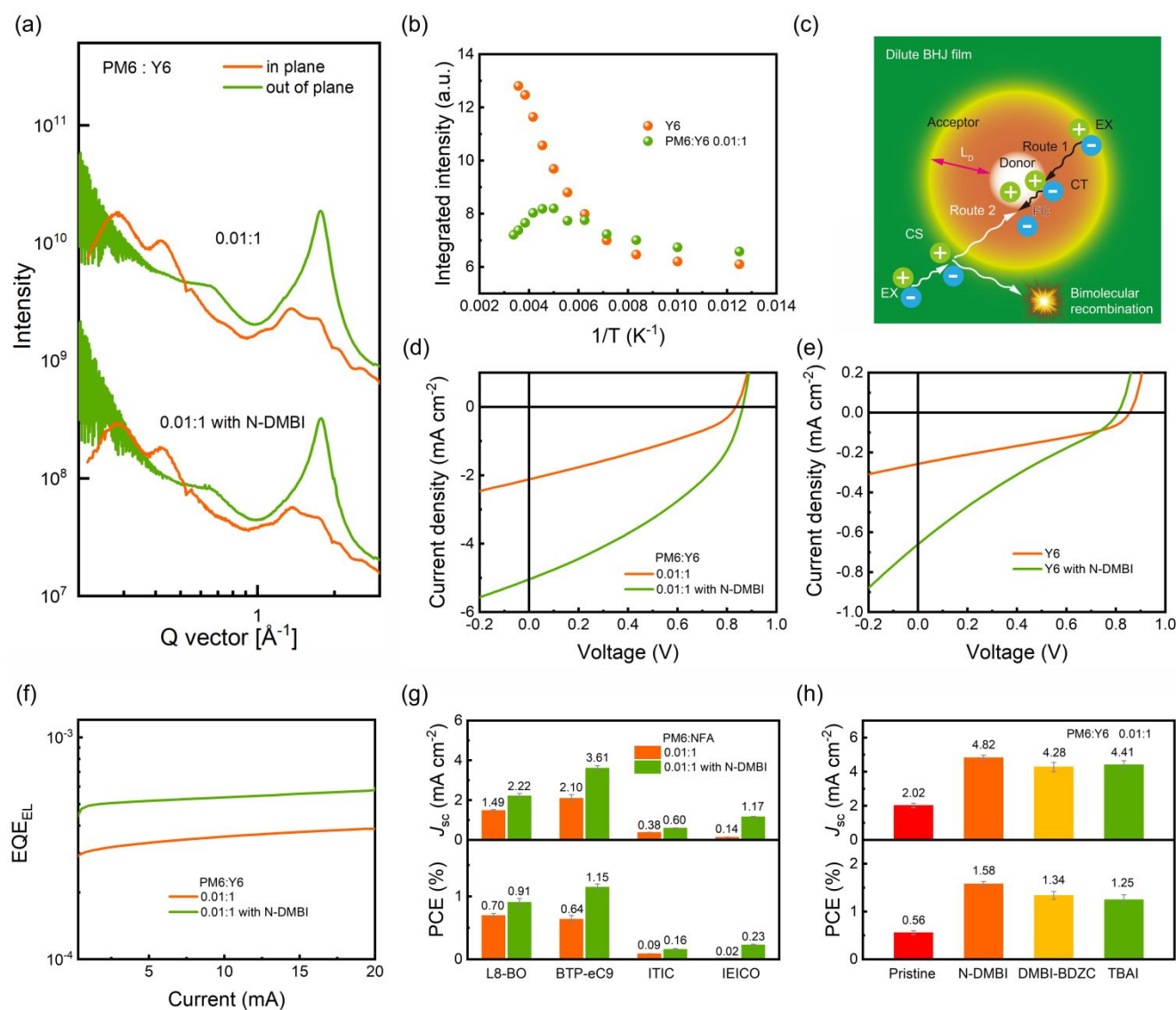


Fig. 3. (a) In plane and out of plane line cuts of the pristine and 0.1 wt% N-DMBI added PM6:Y6 (0.01:1) films. (b) Plots of PL intensities of neat Y6 film and dilute PM6:Y6 (0.01:1) film as a function of temperature from 80 K to room temperature excited at 750 nm. (c) The scheme of the two routes of charge generation in 1% PM6-content dilute BHJ film. Route 1: The EX diffuses to the D/A interface to form CT state, and then splits into FC. Route 2: The EX spontaneously forms CS in Y6, and then moves towards the D/A interface to realize spatial isolation of electron and hole. The CS that fails to reach the D/A interface recombines in bimolecular mode. (d) The J - V curves of the control and 0.1 wt% N-DMBI added PM6:Y6 (0.01:1) devices. (e) The J - V curves of the control and 2 wt% N-DMBI added Y6 devices. (f) The EQE_{EL} measurement of the control and 0.1 wt% N-DMBI added PM6:Y6 (0.01:1) devices. (g) Histograms of J_{sc} and PCE values in PM6:NFA (0.01:1) devices with optimum N-DMBI content. (h) Histograms of J_{sc} and PCE values in PM6:Y6 (0.01:1) devices with various n-dopants at optimum content.

ARTICLE

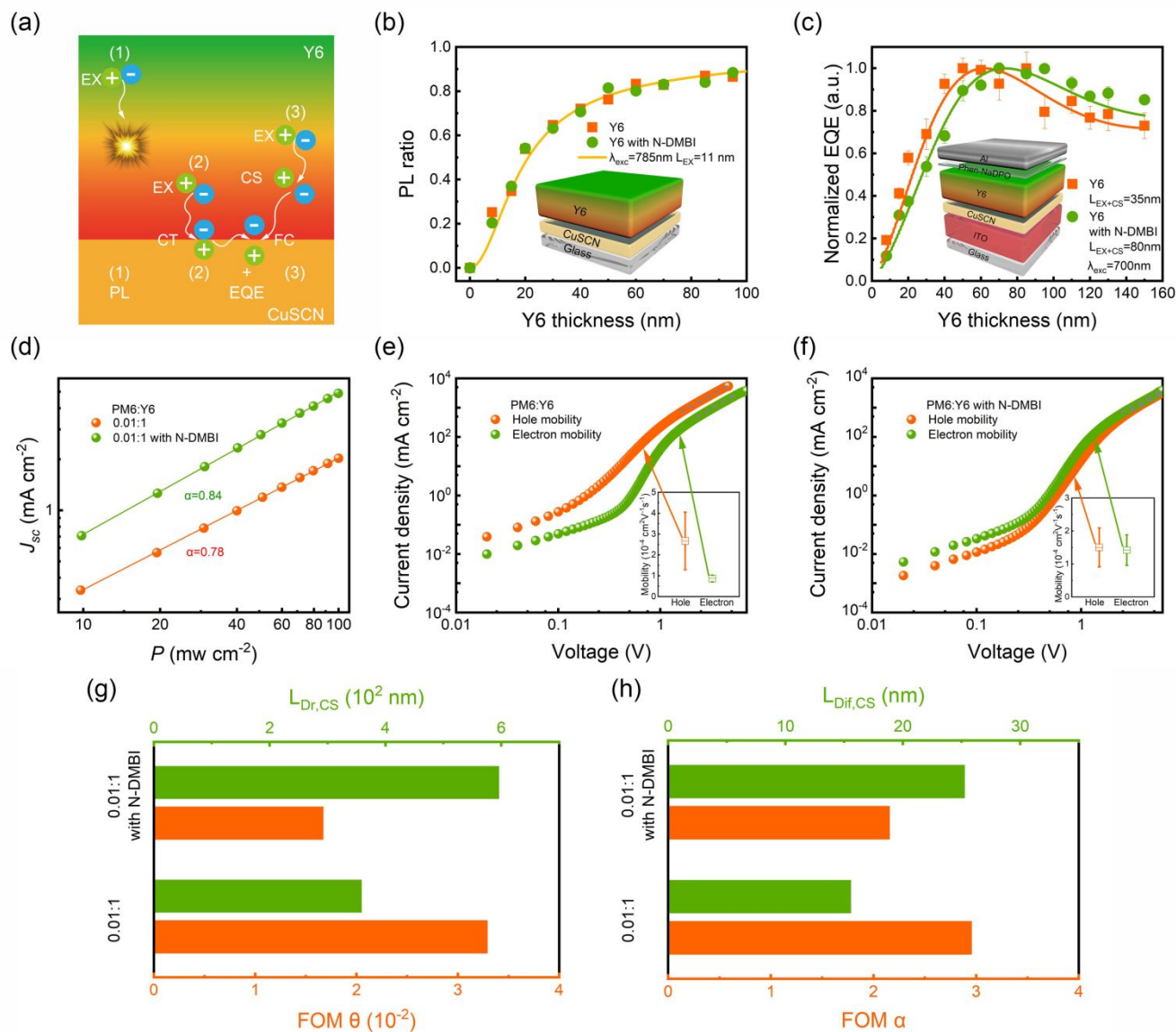


Fig. 4. (a) Scheme of different signals obtained by PL and EQE measurements to evaluate the EX and CS transport lengths. The PL measurement quantifies the EXs that are unable to diffuse to the Y6/CuSCN interface, which reflects the EX diffusion length. The EQE measurement quantifies the EXs and CS states that are able to arrive at the Y6/CuSCN interface, reflecting the total contribution of EXs and CS to transport length. (b) L_{EX} values from the thickness varying PL measurements of the pristine and 0.1 wt% N-DMBI added CuSCN/Y6 bilayer films. The excitation wavelength keeps at 785 nm. The experimental data (diamonds and circles) are fitted (solid lines) for all Y6 thicknesses. The inset is the sample structure of the bilayer films. (c) L_{EX+CS} values from the thickness varying EQE measurements of the pristine and 0.1 wt% N-DMBI added CuSCN/Y6 bilayer devices. The excitation wavelength keeps at 700 nm. The experimental data (diamonds and circles) are fitted (solid lines) for all Y6 thicknesses. The inset is the device architecture of the bilayer devices. (d) Dependence of J_{sc} on the light intensity for the pristine and 0.1 wt% N-DMBI added PM6:Y6 (0.01:1) devices. (e) Hole-only current density and electron-only current density versus voltage curves of the pristine PM6:Y6 (0.01:1) devices. Inset is the average hole and electron mobility values. (f) Hole-only current density and electron-only current density versus voltage curves of 0.1 wt% N-DMBI added PM6:Y6 (0.01:1) devices. Inset is the average hole and electron mobility values. (g) Values of FOM ϑ and $L_{Dr,CS}$ for the pristine and 0.1 wt% N-DMBI added PM6:Y6 (0.01:1) devices. (h) Values of FOM α and $L_{Dif,CS}$ for the pristine and 0.1 wt% N-DMBI added PM6:Y6 (0.01:1) devices.

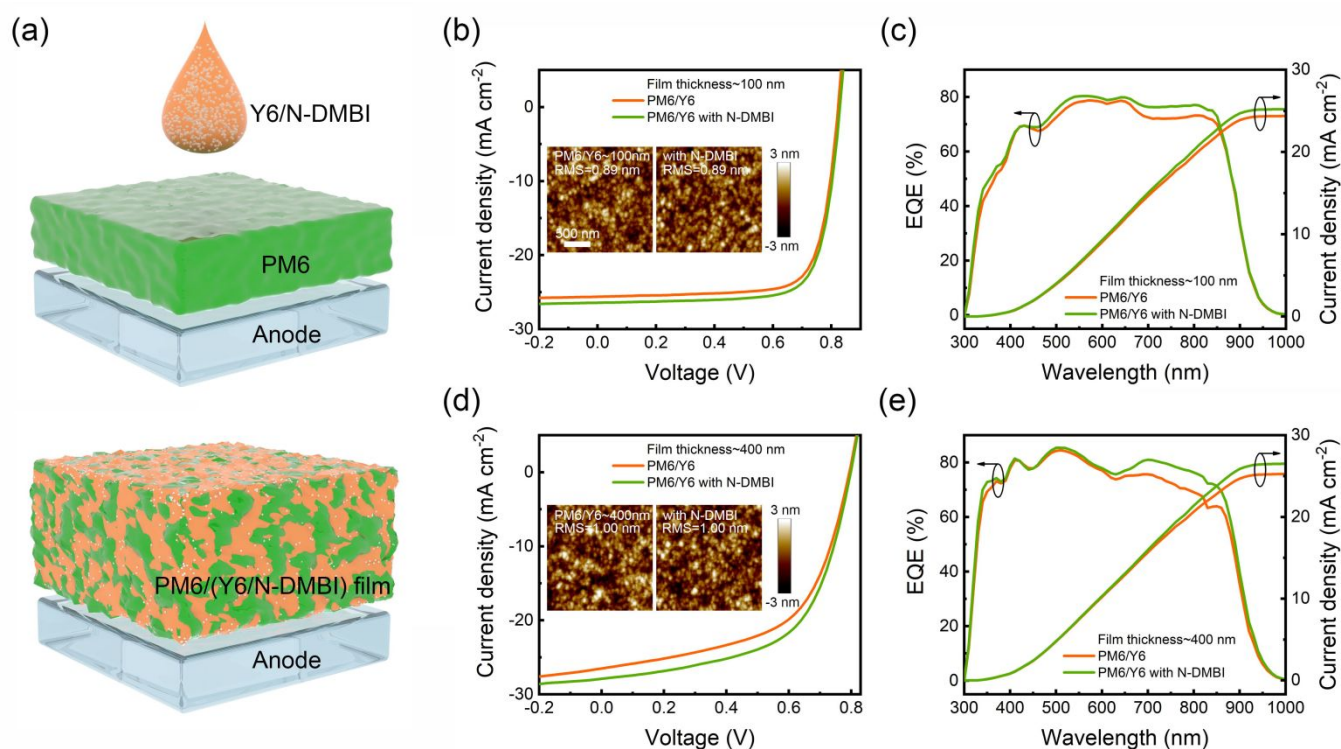


Fig. 5. (a) Scheme of the sequential fabrication procedure for OSCs. The PM6 is firstly deposited onto the substrate, then the N-DMBI/Y6 blend solution in chloroform is spin-coated on. (b and d) The $J-V$ curves of the sequentially fabricated PM6:Y6 BHJ devices with varying active layer film thicknesses: (b) 100 nm film thickness, and (d) 400 nm film thickness. The insets are the corresponding AFM images of blend films. (c and e) The EQE and corresponding integrated current density curves of the sequentially fabricated PM6:Y6 BHJ devices with varying active layer film thicknesses: (c) 100 nm film thickness, and (e) 400 nm film thickness.

Table 1. Photovoltaic performance of sequentially fabricated PM6/Y6 BHJ devices with varying active layer film thicknesses of 100 nm and 400 nm. ^a

Conditions	$V_{oc\ max}$ (V)	FF_{max} (%)	$J_{sc\ max}$ (mA cm ⁻²)	$J_{sc\ avg}$ (mA cm ⁻²)	PCE_{max} (%)	PCE_{avg} (%)	EQE (mA cm ⁻²)
100 nm	0.823	75.9	25.62	25.23±0.37	16.09	15.75±0.18	24.37
100 nm with N-DMBI	0.829	75.9	26.43	26.06±0.46	16.70	16.36±0.19	25.20
400 nm	0.794	56.7	26.51	26.25±0.36	11.88	11.62±0.28	25.26
400 nm with N-DMBI	0.798	58.4	27.91	27.59±0.20	13.03	12.63±0.17	26.51

^aThe maximum and average values were obtained from 10 independent devices.